

Numerical Modeling of Power Take-Off Damping in an Oscillating Water Column Device

Arun Kamath,* Hans Bihs, Øivind A. Arntsen

Department of Civil and Environmental Engineering, Norwegian University of Science and Technology (NTNU), 7491 Trondheim, Norway

International Journal of Marine Energy, 2015, **10** , pp. 1-16.

DOI: <http://dx.doi.org/10.1016/j.ijome.2015.01.001>

Abstract

An Oscillating Water Column (OWC) is a wave energy converter consisting of a partially submerged chamber with an air column over the water column. The work done by the air column under excitation by the incident waves is used to generate electrical energy through a power take-off (PTO) device. The air column is under pressure due to the damping from the PTO device and this pressure is essential for the extraction of wave energy using the OWC. The relationship between the PTO damping and the hydrodynamic efficiency of the OWC provides more insight into the wave energy extraction using an OWC.

In this paper, two-dimensional Computational Fluid Dynamics (CFD) simulations are used to investigate the response of the OWC under different values of damping from the PTO device. The PTO damping on the chamber is represented using a linear pressure drop law with the permeability coefficient derived from Darcy's equation for flow through porous media. The model is validated by comparing the numerical results to experimental data. The influence of the PTO damping on the chamber pressure, the free surface motion, the velocity of the vertical motion of the free surface and the hydrodynamic efficiency of the OWC is studied. The hydrodynamic efficiency is calculated as the ratio of the power delivered at the vent of the OWC to the incident wave power. It is found that the PTO damping needed to attain the maximum OWC hydrodynamic efficiency increases with increasing incident wavelength. The formation of stagnation zones in the water due to high velocities for lower values of PTO damping is found to reduce the hydrodynamic efficiency.

Keywords: Oscillating Water Column; Computational Fluid Dynamics; wave energy; porous media; PTO damping; REEF3D

*Corresponding author, arun.kamath@ntnu.no

Postprint, published in International Journal of Marine Energy, doi:
<http://dx.doi.org/10.1016/j.ijome.2015.01.001>

1 Introduction

An Oscillating Water Column (OWC) device is a renewable energy device used to convert incident wave energy into electrical energy. The device consists of a partially submerged chamber with an air column standing over the water column. The incident waves cause an oscillatory motion of the free surface of the water column, which transfers the motion to the air column. The air is then exhaled and inhaled through a vent in the chamber. A turbine which is the power take-off (PTO) device, is placed over the vent and the motion of the air column across the turbine is used to produce electrical energy. The vent opens to the atmosphere through the PTO device and this results in a pressure drop over the device chamber.

Evans (1978) used a pair of parallel vertical plates to represent an OWC device to obtain a mathematical description of the working principles. A float connected to a spring-dashpot system on the free surface inside the device chamber was used to calculate the efficiency of the device under the assumption of a rigid piston-like motion of the free surface in this work. In practice, the spatial variation of the free surface motion has an effect on the device efficiency. Evans (1982) included the spatial variation of the free surface and derived expressions to calculate power absorption by the device using the volume flow of air and the chamber pressure. It was assumed that the air is incompressible in this scenario and the volume flow of air is equal to the product of the vertical velocity of the free surface and the surface area of the free surface. The hydrodynamic efficiency of the device is then calculated to evaluate the power available at the PTO device in comparison to the incident wave power. So, the device efficiency depends on the chamber pressure and the motion of the free surface. The damping on the OWC chamber due to the PTO device affects the chamber pressure, the free surface motion and consequently, the performance of the OWC.

In experimental investigations, the PTO damping is represented by porous membranes or vents of small dimensions. A study on the PTO device accounting for its linear and non-linear characteristics was presented by Sarmiento and Falcão (1985). They presented analytical expressions for power absorbed by an OWC and the hydrodynamic efficiency considering two-dimensional variation in the free surface. They found that the power take-off was only marginally lesser for a PTO device with non-linear characteristics compared to a device with linear characteristics. Further, Sarmiento (1992) carried out experimental investigations on OWC devices in a wave flume and used filter membranes to represent the pressure drop from a linear PTO device and circular orifice plates to represent non-linear PTO devices to validate the theory presented in Sarmiento and Falcão (1985). The importance of PTO damping on the device performance was also seen in experimental investigations by Thiruvenkatasamy and Neelamani (1997), where the device efficiency was found to be very low when the area of the vent in the device was increased beyond 0.81% of the free surface area.

The relationship between the PTO damping and the OWC hydrodynamics can be used to improve the efficiency of the OWC. Numerical modeling of an OWC including the PTO damping can provide useful insight into the change in the OWC hydrodynamics under different values of PTO damping for different incident wavelengths. This provides the knowledge required to effectively tune the PTO damping with respect to the incident wavelength to obtain the maximum hydrodynamic efficiency. In this direction, Didier et al. (2011) explored the use of porous media theory to model the PTO damping numerically with a linear pressure drop law on a simplified representation of the OWC device as a thin cylinder. López et al. (2014) studied the optimization of turbine induced damping on an OWC device using a CFD

model after validating the model with data from physical model tests. They concluded that each incident wavelength has an optimal damping condition. They varied the PTO damping in the numerical model by changing the dimensions of the OWC vent. The high air velocities resulting from small vent sizes make a simulation very expensive without adding much detail to the hydrodynamics of the OWC. Thus, a different approach that is computationally efficient and represents the hydrodynamics accurately can help to further investigate of the hydrodynamics of an OWC device including the PTO characteristics.

The objective of this study is to investigate the influence of PTO damping on the OWC chamber and on the hydrodynamics in and around the OWC under different incident wave conditions. An open-source CFD model is used to simulate an OWC in a two-dimensional numerical wave tank. First, the numerical model is validated by comparing the chamber pressure, variation of the free surface inside the chamber and the vertical velocity of the free surface with experimental data from Morris-Thomas *et al.* (2007). Then, the variation of the chamber pressure and the free surface inside the chamber is calculated numerically for different wavelengths, wave heights and PTO damping. The effect of the PTO damping on the chamber pressure, free surface and power absorption under different values of incident wavelengths and wave heights on the OWC is studied.

2 Numerical Model

2.1 Governing Equations

The open-source CFD model, REEF3D Alagan Chella *et al.* (2015) uses the incompressible Reynolds-averaged Navier-Stokes (RANS) equations along with the continuity equation to solve the fluid flow problem:

$$\frac{\partial u_i}{\partial x_i} = 0 \quad (1)$$

$$\frac{\partial u_i}{\partial t} + u_j \frac{\partial u_i}{\partial x_j} = -\frac{1}{\rho} \frac{\partial p}{\partial x_i} + \frac{\partial}{\partial x_j} \left[(\nu + \nu_t) \left(\frac{\partial u_i}{\partial x_j} + \frac{\partial u_j}{\partial x_i} \right) \right] + g_i \quad (2)$$

where u is the velocity averaged over time t , ρ is the fluid density, p is the pressure, ν is the kinematic viscosity, ν_t is the eddy viscosity and g is the acceleration due to gravity.

The pressure is determined using Chorin's projection method Chorin (1968) and the resulting Poisson pressure equation is solved using a preconditioned BiCGStab solver van der Vorst (1992). Turbulence modeling is carried out by the two-equation k - ω model proposed by Wilcox (1994). The transport equations for the turbulent kinetic energy, k and the specific turbulent dissipation rate, ω are given by:

$$\frac{\partial k}{\partial t} + u_j \frac{\partial k}{\partial x_j} = \frac{\partial}{\partial x_j} \left[\left(\nu + \frac{\nu_t}{\sigma_k} \right) \frac{\partial k}{\partial x_j} \right] + P_k - \beta_k k \omega \quad (3)$$

$$\frac{\partial \omega}{\partial t} + u_j \frac{\partial \omega}{\partial x_j} = \frac{\partial}{\partial x_j} \left[\left(\nu + \frac{\nu_t}{\sigma_\omega} \right) \frac{\partial \omega}{\partial x_j} \right] + \frac{\omega}{k} \alpha P_k - \beta \omega^2 \quad (4)$$

$$\nu_t = \frac{k}{\omega} \quad (5)$$

where, P_k is the production rate, ν_t is the eddy viscosity and closure coefficients $\sigma_k = 2$, $\sigma_\omega = 2$, $\alpha = 5/9$, $\beta_k = 9/100$, $\beta = 3/40$. The oscillatory nature of wave propagation results in large gradients or strain in the flow. The production terms in the turbulence model are directly dependent on the strain. This results in an unphysical overproduction of turbulence in the case of wave propagation. This is avoided by introducing a stress limiter in the definition of eddy viscosity based on the Bradshaw et al. (1967) assumption and as demonstrated by Durbin (2009):

$$\nu_t \leq \sqrt{\frac{2}{3}} \frac{k}{|\mathbf{S}|} \quad (6)$$

where \mathbf{S} represents the source terms in the transport equations.

In a two-phase numerical model, the large difference between the density of air and water results in a large strain at the free surface. The free surface in reality is a natural boundary which dampens the eddy viscosity but this effect is not accounted for by the k - ω model. The overproduction of turbulence in this case is reduced using free surface turbulence damping using a source term in the specific turbulent dissipation equation as shown by Egorov (2004):

$$S_n = \left(\frac{6 B \nu}{\beta dx^2} \right)^2 \beta dx \delta(\phi) \quad (7)$$

where, model parameter B is set to 100.0 and dx is the grid size. The damping is carried out only at the free surface using the Dirac delta function, $\delta(\phi)$.

2.2 Discretization Schemes

Discretization of the convective terms in the RANS equations is carried out using the fifth-order finite difference Weighted Essentially Non-Oscillatory (WENO) scheme proposed by Jiang and Shu (1996) and the Hamilton-Jacobi formulation of the WENO scheme Jiang and Peng (2000) is used to discretize the level set function ϕ , turbulent kinetic energy k and the specific turbulent dissipation rate ω . The scheme is a minimum third-order accurate in the presence of large gradients and shocks and provides the accuracy required to model complex free surface flows. A Total Variation Diminishing (TVD) third-order Runge-Kutta scheme Shu and Osher (1988) is used for time advancement of momentum equation, the level set function and the reinitialisation equation. The time steps in the simulation are determined using an adaptive time stepping strategy satisfying the Courant-Frederick-Lewy (CFL) criterion. The time advancement of k and ω is carried out using a first-order implicit scheme as these terms are mainly source term driven with a low influence from convective terms. The implicit treatment of these terms avoids small time steps resulting from large source terms in the turbulence model. The diffusion terms of the velocities are also removed from the CFL criterion by using an implicit scheme to handle these terms.

The numerical model uses a uniform Cartesian grid for spatial discretization and the implementation of higher-order finite difference schemes is straight-forward. The Immersed Boundary Method (IBM) Berthelsen and Faltinsen (2008) is used to handle the boundary conditions for complex geometries. This method extrapolates values from the fluid into the solid region using ghost cells. The numerical model is completely parallelised using the MPI library and can be executed on high performance computing systems.

2.3 Free Surface

The free surface in the numerical wave tank is obtained using the level set method, where the interface between two fluids is represented by the zero level set of the level set function, $\phi(\vec{x}, t)$. The level set function gives the closest distance of each point in the domain from the interface and the two fluids are distinguished by the sign of the function. This signed distance function is defined as:

$$\phi(\vec{x}, t) \begin{cases} > 0 & \text{if } \vec{x} \text{ is in phase 1} \\ = 0 & \text{if } \vec{x} \text{ is at the interface} \\ < 0 & \text{if } \vec{x} \text{ is in phase 2} \end{cases} \quad (8)$$

The definition of the level set function makes it continuous across the interface and provides a sharp representation of the free surface. The level set function is convected under the velocity field in the wave tank. The signed distance property of the function is lost by the motion of the free surface and it is restored by reinitializing the function after every iteration using the partial differential equation based procedure by Peng *et al.* (1999).

2.4 Numerical Wave Tank

Wave generation and absorption in the numerical wave tank is carried out using the relaxation method Larsen and Dancy (1983). In this method, relaxation functions are used to moderate the computational values with an analytical solution from wave theory in specific parts of the numerical wave tank reserved for wave generation and absorption, called relaxation zones. The relaxation method has been implemented by several authors like Mayer *et al.* (1998), Engsig-Karup (2006) and Jacobsen *et al.* (2012). The relaxation functions presented by Engsig-Karup (2006) listed in Eq. (9) are implemented in the numerical model using three relaxation zones as illustrated in Fig. (1).

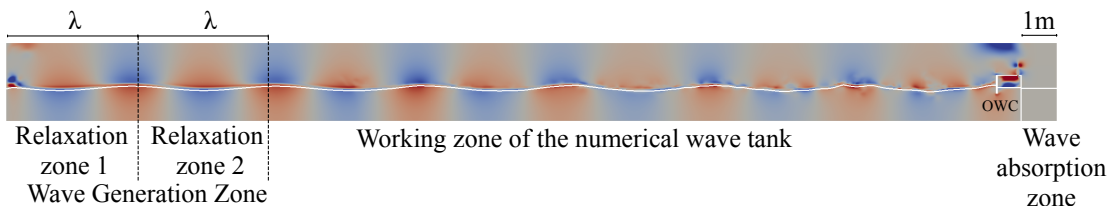


Figure 1: Numerical wave tank showing the relaxation zones and the OWC

$$\Gamma(x) \begin{cases} = -2x^3 + 3x^2 & \text{for relaxation zone 1} \\ = -2(1-x)^3 + 3(1-x)^2 & \text{for relaxation zone 2} \\ = (1-x)^6 & \text{for wave absorption zone} \end{cases} \quad (9)$$

where $\Gamma(x)$ is called the relaxation function and $x \in [0, 1]$ is the length scale along the relaxation zone.

The waves are generated in the first relaxation zone, where the analytical values for velocity and free surface elevation from wave theory are gradually prescribed into the numerical wave tank. The second zone, placed right after the first zone, prevents reflections from the working zone of the wave tank from affecting the wave generation. The working zone of the wave

tank is next to the second relaxation zone and the objects to be studied are placed here. The third relaxation zone is placed at the far end of the numerical wave tank and is responsible for wave absorption. In this zone, the computational value of velocity is smoothly brought to zero, the free surface elevation returned to the still water level and the pressure to its hydrostatic value. In this way, the wave energy is smoothly removed from the numerical wave tank without reflections from the boundary affecting the results in the working zone. The relaxation functions prescribe the values for the velocity and the free surface elevation in the relaxation zones using Eq. (10) with the corresponding relaxation functions.

$$\begin{aligned} u_{relaxed} &= \Gamma(x)u_{analytical} + (1 - \Gamma(x))u_{computational} \\ \phi_{relaxed} &= \Gamma(x)\phi_{analytical} + (1 - \Gamma(x))\phi_{computational} \end{aligned} \quad (10)$$

In this way, the required values are introduced into the numerical wave tank gradually, ensuring smooth wave generation and absorption.

3 Hydrodynamic Efficiency of an OWC device

Hydrodynamic efficiency of an OWC provides a measure of the wave power available at the OWC chamber vent for the production of electrical energy by the PTO device. The hydrodynamic efficiency is used to investigate the effect of the OWC geometric configuration and PTO characteristics on the wave power absorption. The wave energy incident on the device chamber causes the free surface inside the chamber to oscillate and this energy is transferred to the air column above it. The presence of a PTO device results in a pressure in the chamber and the wave power absorbed is calculated as the work done by the air column under this pressure. The power available at the turbine P_{out} , per wave cycle of period T is measured as the time average of the product of the chamber pressure, p_c and the volume of air flowing through the vent q Evans (1982):

$$P_{out} = \frac{1}{T} \int_0^T p_c(t) q(t) dt \quad (11)$$

Due to the small scale of the device and the chamber pressures developed, the air in the chamber is considered to be incompressible and the volume of air flowing through the vent is calculated as the product of the velocity of the free surface and the cross-sectional area of the chamber. The value for pressure is available at every point in the chamber for every time step from the Poisson pressure equation. So, the power available at the vent can be easily calculated.

The incident wave energy flux, E_{in} is calculated as the product of energy content of the wave and the group velocity of the wave:

$$E_{in} = \frac{1}{2} \rho g a_0^2 c_g \quad (12)$$

where a_0 is the incident wave amplitude and c_g is the group velocity.

This provides the wave power incident per meter width of the device and the wave power incident on the device is calculated by multiplying the width of the device, l . The hydrodynamic efficiency of the device is then calculated as the ratio between the wave power available at the vent to the incident wave power:

$$\eta_{owc} = \frac{P_{out}}{E_{in} l} \quad (13)$$

4 Modeling the PTO damping

The PTO damping on the device chamber from the PTO device is modeled using the porous media flow relation. A PTO device such as the Wells turbine which has linear pressure drop characteristics can be effectively represented by a linear pressure drop law in model testing Sarmiento and Falcão (1985) Falcão and Henriques (2014). The porous media in the vent models the PTO damping, accounting for the pressure and free surface motion in the OWC chamber in the numerical model. A linear pressure drop law is implemented in the numerical model as:

$$\frac{\Delta p}{L} = -C\mu q \quad (14)$$

where μ is the dynamic viscosity of the fluid, Δp is the pressure drop across the vent, C is the permeability coefficient and L is the length along the direction of the flow. The permeability coefficient $C = 1/k_p$ is determined using Darcy's law for flow through porous media:

$$q = \frac{-k_p A_{cs} \Delta p}{\mu L} \quad (15)$$

where k_p is the intrinsic permeability, q is the flow rate and A_{cs} is the cross-sectional area. In this study, the flow rate q and the pressure drop across the vent Δp is known from the experimental data Morris-Thomas et al. (2007). The values of the pressure drop and of the volume flow of air across the vent from the experiments under conditions close to resonance are used. The variables A_{cs} and L are known from the device configuration and μ is a known constant. Thus, the value of intrinsic permeability can be determined by solving Eq. (15) for k_p , which is used to determine the permeability coefficient C . In a practical scenario, the pressure drop and air flow across the turbine is known from the turbine characteristics and those values can be used to investigate the performance of the device. The porous media relation is then used at the vent to model PTO damping. In this way, the PTO damping in the numerical model is represented independent of the dimensions of the vent size and the influence of PTO damping on the device can be studied by varying the value of C .

5 Results and Discussion

At first, the grid size for accurate wave generation and propagation in the numerical wave tank is determined using a grid refinement study. Linear waves of wavelength $\lambda = 4.0\text{m}$ and height $H = 0.12\text{m}$ with wave steepness $\xi = H/\lambda = 0.03$ are generated in a two-dimensional numerical wave tank 20m long, 2.20m high and with a water depth $d = 0.92\text{m}$. The grid sizes are varied between $dx = 0.1\text{m}$, $dx = 0.05\text{m}$, $dx = 0.025\text{m}$ and $dx = 0.01\text{m}$. It is seen from Fig. 2 that the waveform converges to the analytical envelope expected from the linear wave theory at a grid size of 0.025m. This grid size is then used for all the numerical simulations carried out in the study.

5.1 Validation

The experimental setup used in Morris-Thomas et al. (2007) is simulated to validate the numerical model. The experiments were carried out at the University of Western Australia in a wave tank of length 50m and width 1.5m. The model OWC was placed 37.5m from the

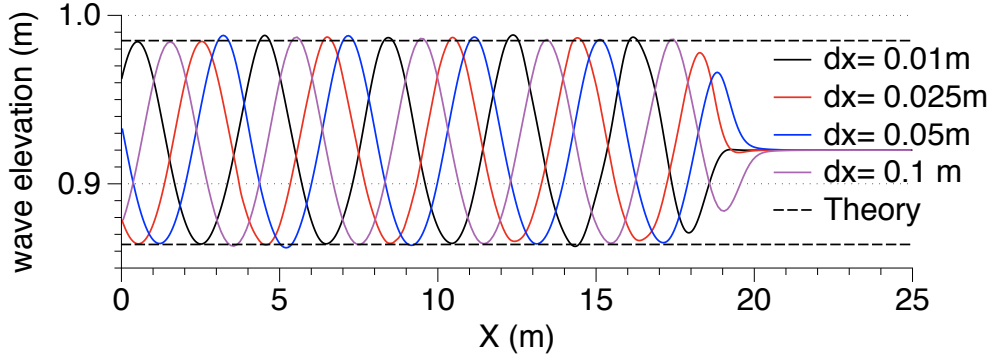


Figure 2: Grid convergence for incident waves with $\lambda = 4.07\text{m}$ and $H = 0.12\text{m}$

wavemaker. The PTO device was represented by a rectangular vent of width $b_v = 0.005\text{m}$ in the roof of the chamber 0.05m from the rear wall. The same geometry is replicated in the numerical simulations with a minor change in the representation of the PTO device, where the vent width b_v is set to 0.05m . The pressure drop equation (Eq. 14) is used to determine the value of C required to obtain the same pressure drop across a vent of width $b_v = 0.05\text{m}$ as that across a vent of width $b_v = 0.005\text{m}$ in the experiments. Using the experimental data for $\lambda = 4.07\text{m}$, where $\Delta p = 500\text{Pa}$, $q = 0.11\text{m}^3/\text{s}$ in Eq. 14, results in $C_{exp} = 5 \times 10^8\text{m}^{-2}$ for providing the same pressure drop and volume flux across a vent of width $b_v = 0.05\text{m}$ in the numerical model. A schematic diagram of the setup is shown in Fig. 3. The porous media in the numerical model is validated by simulating different incident wavelengths on the OWC with $C_{exp} = 5 \times 10^8\text{m}^{-2}$ used for the porous layer in the vent.

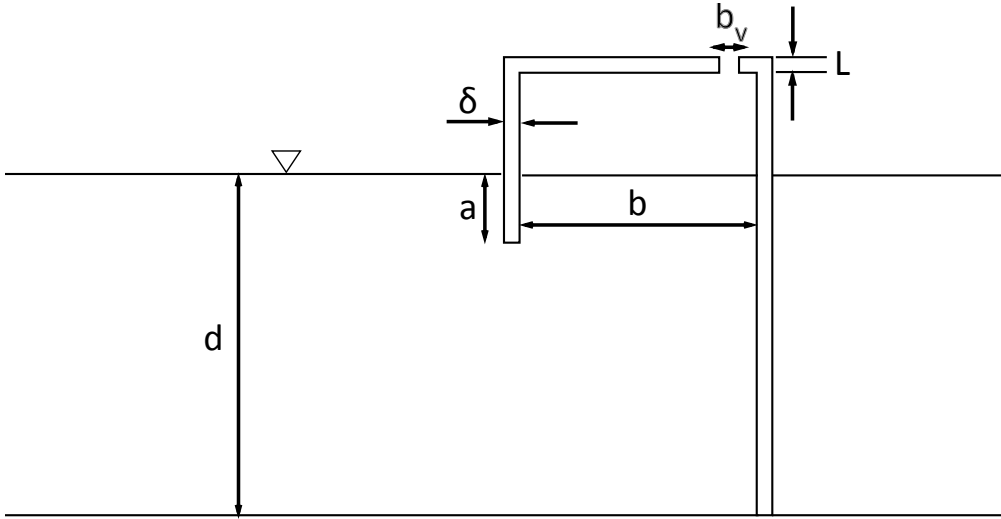


Figure 3: Configuration of the OWC device

In the first case, waves of wavelength $\lambda = 4.07\text{m}$ and height $H = 0.12\text{m}$ are incident on the OWC device in a water depth of $d = 0.92\text{m}$. The device shows resonant response and has the maximum efficiency in the experiments for this wavelength. The device has a front wall

draught $c = 0.15\text{m}$ and front wall thickness $\delta = 0.05\text{m}$, a chamber length $b = 0.64\text{m}$ and a chamber height of 1.275m . The first and the second relaxation zones are kept one wavelength long and the wave absorption zone is 1m long. The device covers the entire width of the tank and the wave absorption zone does not have an important influence on the simulation. The variation of the chamber pressure $p_c(t)$ and the free surface at the center of the chamber $\eta(t)$ is calculated and compared with the experimental observations in Fig. 4a and 4b respectively. The velocity of the free surface motion, w_{fs} is calculated using the free surface motion in the numerical simulations and experimental data and presented in Fig. 4c. A good agreement is seen between the numerical results and the experimental observations in these figures. This wavelength of $\lambda = 4.07\text{m}$ corresponds to the resonant frequency of the OWC chamber and the maximum efficiency was observed in the experiments for this incident wavelength. In spite of being the resonant condition, the free surface oscillations are not amplified (Fig. 4b) due to the PTO damping on the chamber but a large part of the incident wave energy is transferred from the water column to the air column resulting in a maximum efficiency at this incident wavelength.

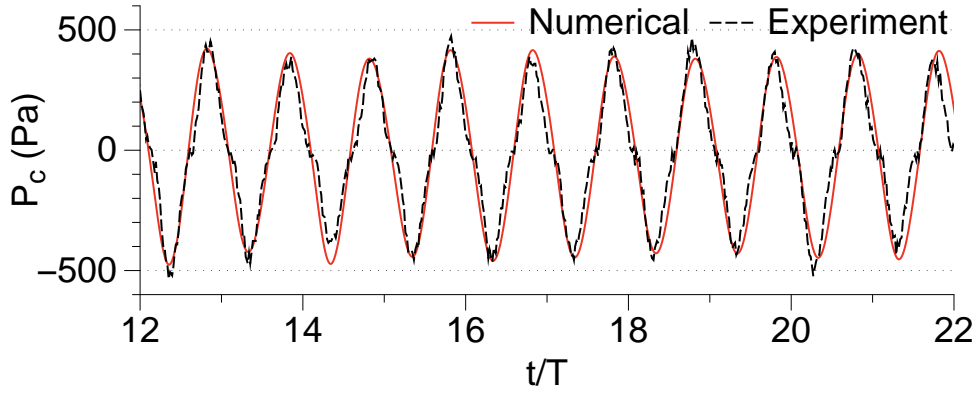
Next, simulations are carried out with incident wavelengths of $\lambda = 5.07\text{m}$ and $\lambda = 2.90\text{m}$ with a wave height of $H = 0.12\text{m}$. These wavelengths lie on either sides of the resonant wavelength and are used to study the device performance away from resonance. The variation of the chamber pressure p_c , free surface at the centre of the chamber η and the velocity of the free surface w_{fs} for $\lambda = 5.07\text{m}$ is presented in Fig. 5 and a good agreement is seen between the numerical and experimental results. Similarly, a good agreement is seen between the numerical results and the experimental observations for the variation of the chamber pressure p_c , the free surface in the chamber η and the velocity of the free surface w_{fs} for $\lambda = 2.90\text{m}$ in Fig. 6. The free surface motion in these cases is further damped compared to the free surface motion in the resonant case.

It seen that a good representation of the fluid dynamics in the device chamber is obtained from the numerical model. It is also confirmed that a value of $C_{exp} = 5 \times 10^8\text{m}^{-2}$ provides the same pressure drop on a vent of width $b_v = 0.05\text{m}$ as that provided by a vent of width $b_v = 0.005\text{m}$ in the experiments. Thus, C_{exp} is taken to be the standard value of damping and then varied to study the influence of the PTO damping on the performance of the device. The cross-sectional area of the vent in the numerical model is larger than in the experiments and is higher than 0.81% of the free surface area. The damping provided by the vent is insufficient to develop the chamber pressure necessary for energy extraction from the device Thiruvengatasamy and Neelamani (1997) and the porous media in the vent is responsible for the PTO damping.

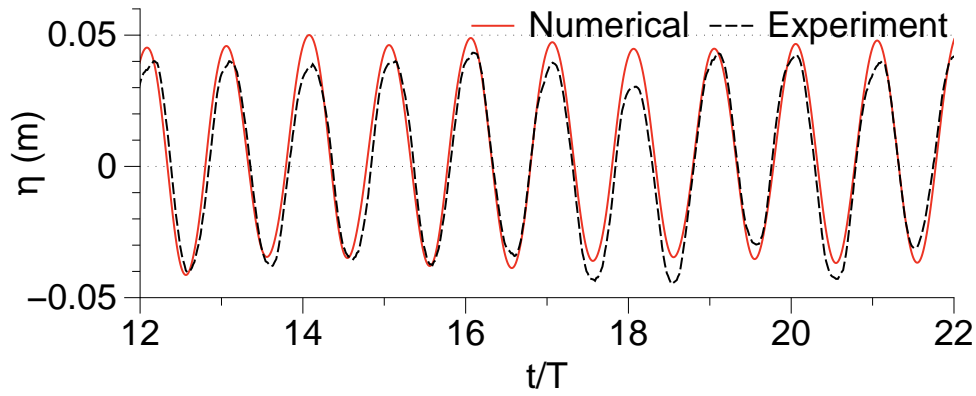
5.2 Effect of PTO damping

In order to study the effect of PTO damping on the performance of the OWC device, the permeability coefficient C in Eq. (14) is varied. Simulations are carried out with values of C_0 , C_1 , C_2 , C_3 , C_4 , C_6 and C_{10} with values listed in Table (1) to investigate the effect of PTO damping. The case without PTO damping (C_0) represents an OWC with a pressure drop from a vent of width $b_v = 0.05\text{m}$. A total of 72 simulations with the 8 different values of the permeability coefficient C , for three different incident wavelengths λ are carried out for wave heights $H = 0.06$, $H = 0.12$ and a constant wave steepness $\xi = 0.03$.

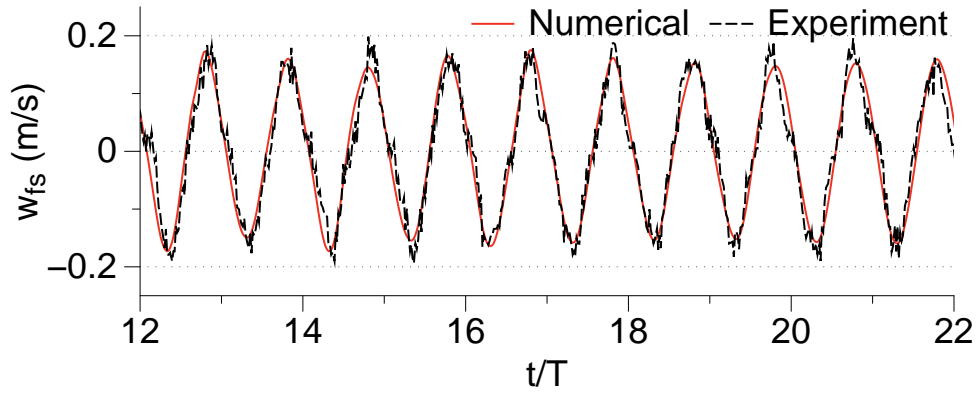
First, simulations are carried out with an incident wave height of $H = 0.06\text{m}$ for wave-



(a) variation of chamber pressure

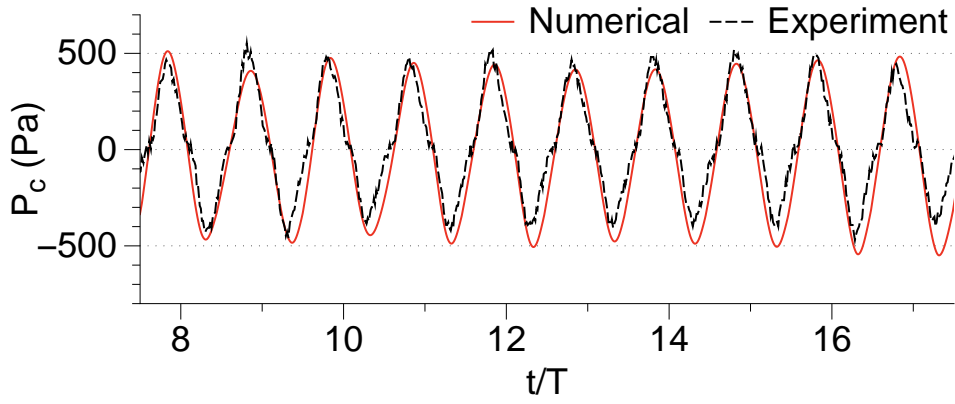


(b) relative free surface elevation at the centre of the chamber

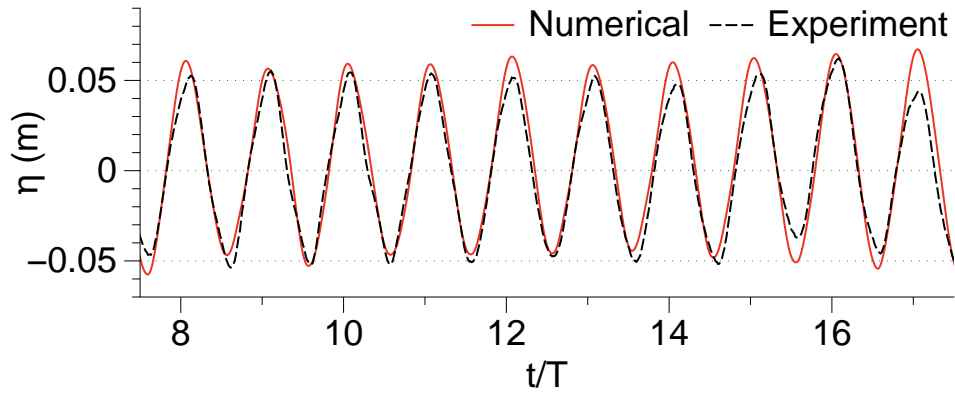


(c) velocity of the free surface

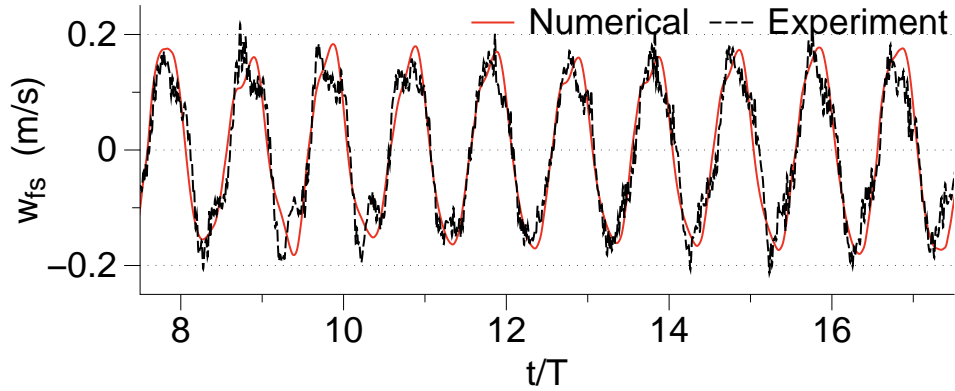
Figure 4: Comparison experimental and numerical results for chamber pressure, free surface elevation and velocity of the free surface inside the chamber for $\lambda = 4.07\text{m}$



(a) variation of chamber pressure

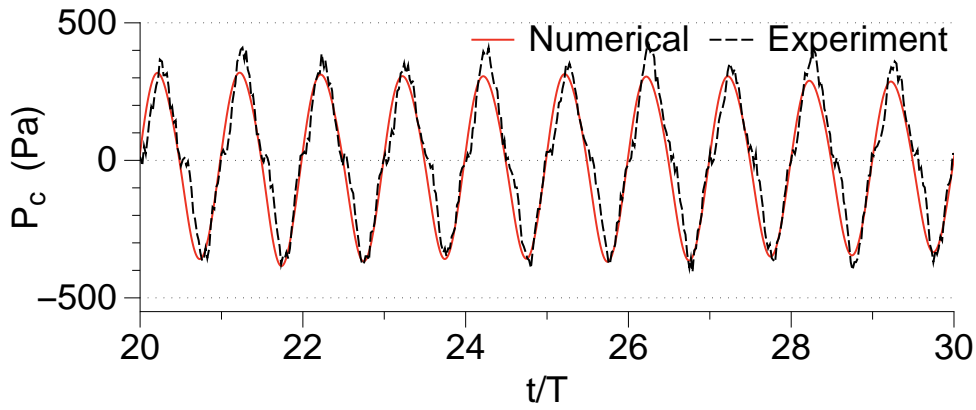


(b) relative free surface elevation at the centre of the chamber

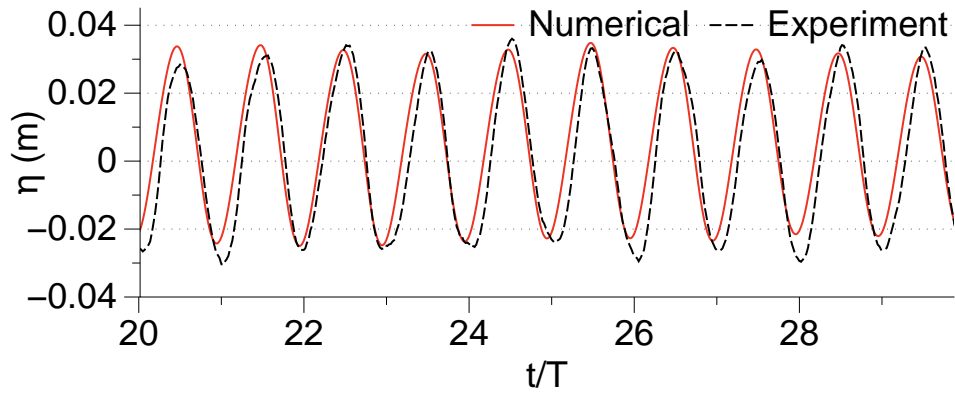


(c) velocity of the free surface

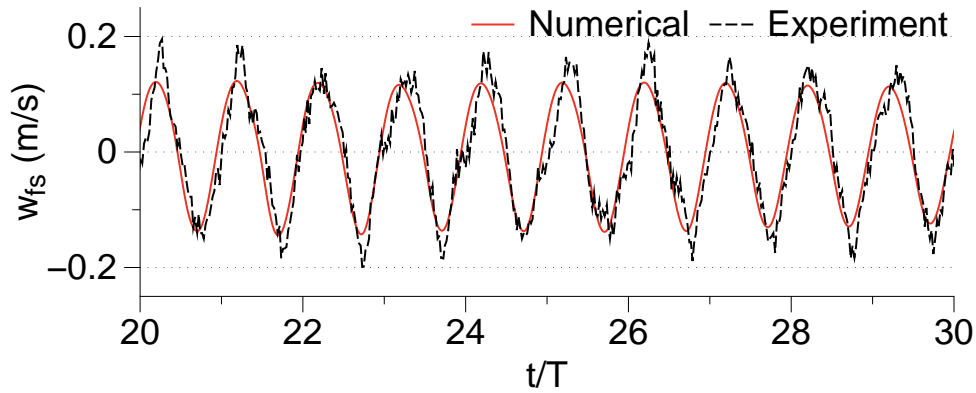
Figure 5: Comparison experimental and numerical results for chamber pressure, free surface elevation and velocity of the free surface inside the chamber for $\lambda = 5.07\text{m}$



(a) variation of chamber pressure



(b) relative free surface elevation at the centre of the chamber



(c) velocity of the free surface

Figure 6: Comparison experimental and numerical results for chamber pressure, free surface elevation and velocity of the free surface inside the chamber for $\lambda = 2.90\text{m}$

C	value	implication
C_0	0	No damping
C_1	1×10^8	low damping
C_2	2×10^8	low damping
C_3	3×10^8	moderate damping
C_4	4×10^8	moderate damping
C_{exp}	5×10^8	from experimental data
C_6	6×10^8	high damping
C_{10}	10×10^8	high damping

Table 1: List of damping values used in the simulations

lengths $\lambda = 2.90\text{m}$, 4.07m and 5.07m with permeability coefficients C_0 to C_{10} . The amplitudes of the chamber pressure p_c , the relative free surface in the chamber a/a_0 , the vertical velocity of the free surface motion inside the chamber w_{fs} and the hydrodynamic efficiency of the OWC η_{owc} for the different incident wavelengths simulated are presented in Fig. (7). The chamber pressure is seen to increase as the value of C is increased from C_0 to C_{10} in Fig. 7a. The longest wavelength simulated, $\lambda = 5.07\text{m}$ results in the largest chamber pressure for all values of C . The damping of the free surface motion inside the OWC chamber is seen in Fig. 7b. The relative free surface motion is about two times the incident amplitude for $\lambda = 5.07\text{m}$ under zero damping (C_0) and reduces to about 0.4 times the incident amplitude under high damping of C_{10} . For an incident wavelength of $\lambda = 4.07$, the maximum free surface elevation is $1.5a_0$ at C_0 and reduces to $0.35a_0$ at C_{10} . The free surface elevation inside the chamber reduces from $1.35a_0$ at C_0 to $0.2a_0$ at C_{10} for an incident wavelength of $\lambda = 2.90\text{m}$. Thus, the free surface oscillations reduce with decreasing incident wavelength and increasing values of PTO damping. The vertical velocity of the free surface motion shows a similar trend where the the velocity w_{fs} decreases with a decrease in wavelength and an increase in the PTO damping.

The hydrodynamic efficiency of the OWC initially increases with increasing PTO damping and then reduces after attaining a maximum value. In the case of the shortest wavelength simulated, $\lambda = 2.90\text{m}$, η_{owc} reaches a maximum of 0.745 at C_3 and then reduces to 0.37 at C_{10} . The hydrodynamic efficiency for an incident wavelength of $\lambda = 4.07\text{m}$ reaches a maximum of 0.83 at C_4 and reduces to 0.61 at C_{10} . For an incident wavelength of $\lambda = 5.07\text{m}$, a maximum value of 0.75 is seen for C_5 and the hydrodynamic efficiency reduces to 0.59 for C_{10} . Thus, it is seen that an increase in PTO damping results in an increase in the chamber pressure p_c and a decrease in the free surface elevation and the velocity of the free surface motion inside the OWC chamber. The hydrodynamic efficiency η_{owc} increases with increasing PTO damping, reaches a maximum and then reduces with further increase in the PTO damping for all the wavelengths. It is also observed that the PTO damping resulting in the maximum efficiency for a given wavelength increases with increasing incident wavelength.

Next, simulations are carried out with an incident wave height of $H = 0.12\text{m}$. The chamber pressure increases with increasing PTO damping in Fig. 8a. The free surface amplitude and the velocity of the free surface in the OWC chamber reduce with an increase in the PTO damping in Figs. 8b and 8c. This variation of the chamber pressure, the relative free surface and the vertical velocity of the free surface with the PTO damping is similar to that seen for an incident wave height of $H = 0.06\text{m}$. The variation in the hydrodynamic efficiency of

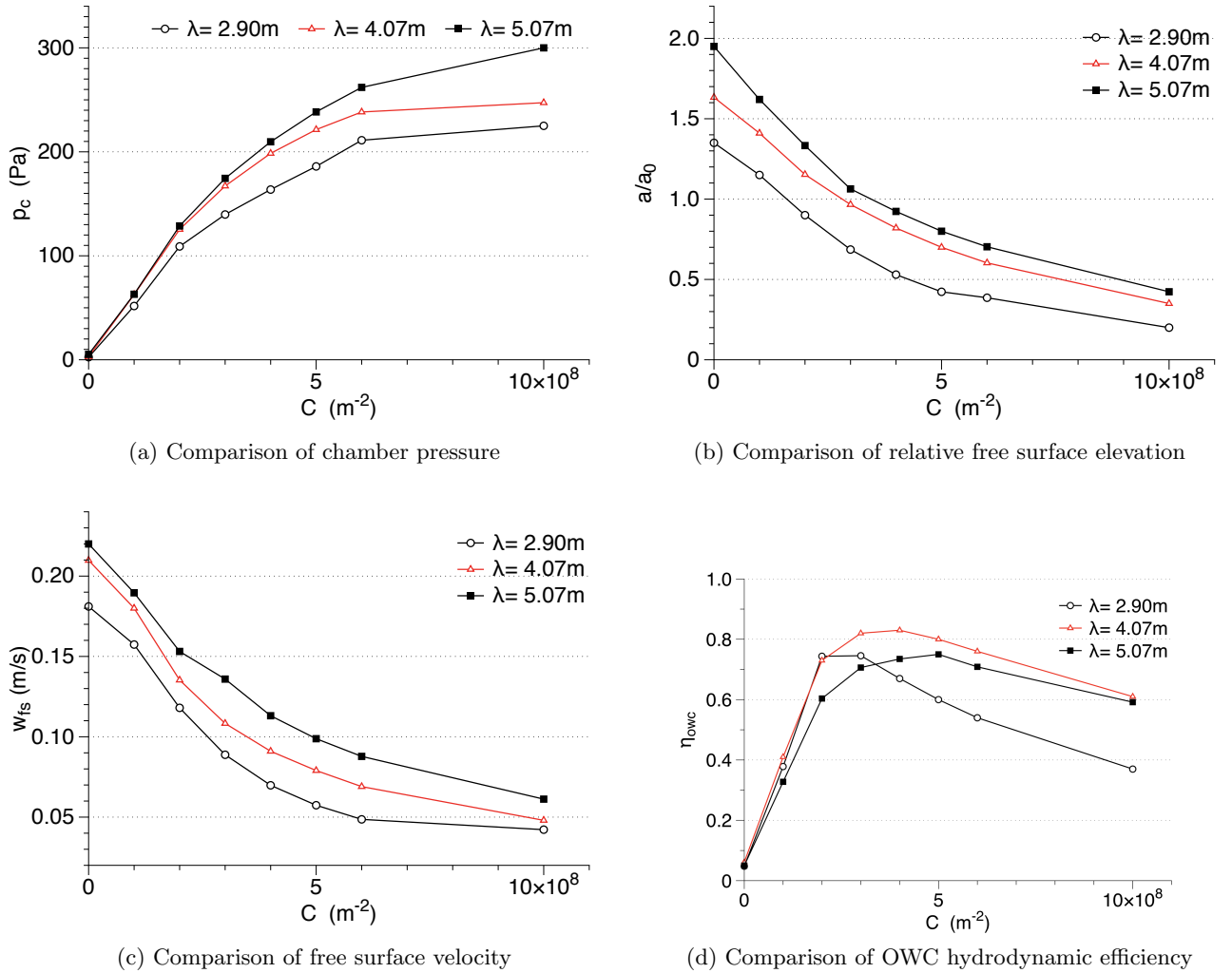


Figure 7: Variation of chamber pressure, relative free surface amplitude, free surface velocity and OWC hydrodynamic efficiency for different wavelengths under different values of C for a constant wave height $H = 0.06$

the OWC with the PTO damping for the different wavelengths in Fig. 8d is similar but with certain differences to that seen for $H = 0.06$ m. The hydrodynamic efficiency increases with increase in PTO damping, reaches a maximum and reduces with further increase in the PTO damping as seen for $H = 0.06$ m previously. Also, the maximum efficiencies are attained at the same values of C for each of the wavelengths. The difference is that the maximum efficiencies for every wavelength at every value of PTO damping is lower than that seen for $H = 0.06$ m. Thus, it is seen that the hydrodynamic efficiency of the device reduces with increasing wave amplitude for the same wavelength and damping conditions.

The investigations with a constant wave height for different wavelengths results in different wave steepnesses for the different cases. The wave steepness can influence the wave interaction with the OWC device. So, the influence of the PTO damping over various wavelengths for

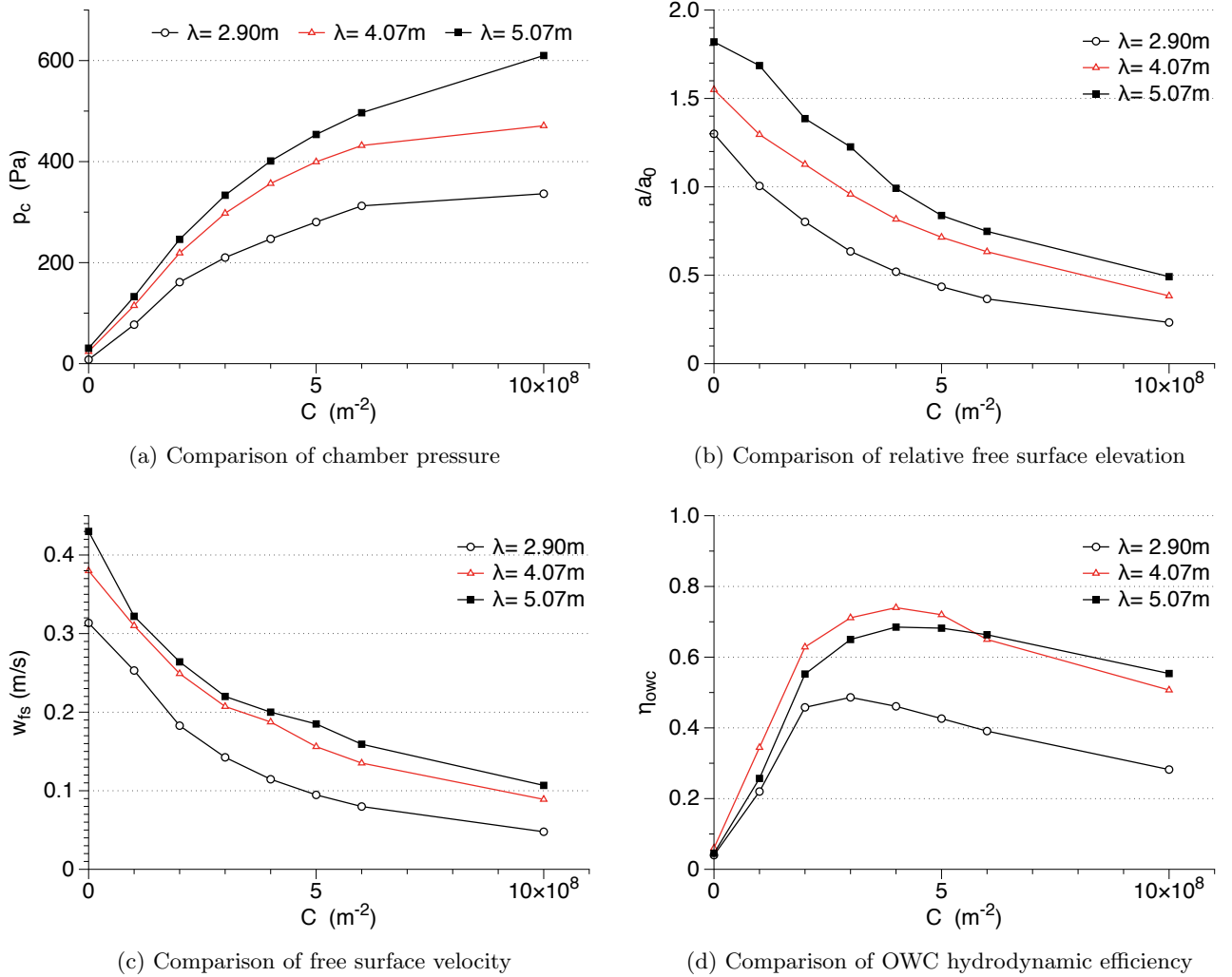


Figure 8: Variation of chamber pressure, relative free surface amplitude, free surface velocity and OWC hydrodynamic efficiency for different wavelengths under different values of C for a constant wave height $H = 0.12$

a constant wave steepness of $\xi = 0.03$ is investigated. The variation of p_c , a/a_0 and w_{fs} presented in Fig. 9 are similar to that seen previously for both $H = 0.06$ and $H = 0.12$ m. The curves for $\lambda = 4.07$ m and $\lambda = 5.07$ m lie close to each other and away from the curve for $\lambda = 2.90$ m because the incident wave heights are proportional to the wavelengths in these cases.

The hydrodynamic efficiency of the OWC for different wavelengths is shown in Fig. 9d. The efficiency for $\lambda = 2.90$ in this case is lower than that computed for $H = 0.06$ m but higher than in the case of $H = 0.06$ m. The incident wave steepness $\xi = 0.03$ for $\lambda = 2.90$ m results in a wave height of $H = 0.087$ m in this case. Thus, the decrease in hydrodynamic efficiency with an increase in incident wave height is further affirmed. In the case of $\lambda = 4.07$, the wave height is $H = 0.122$ m resulting in an efficiency curve similar to that for $H = 0.12$ m and lower

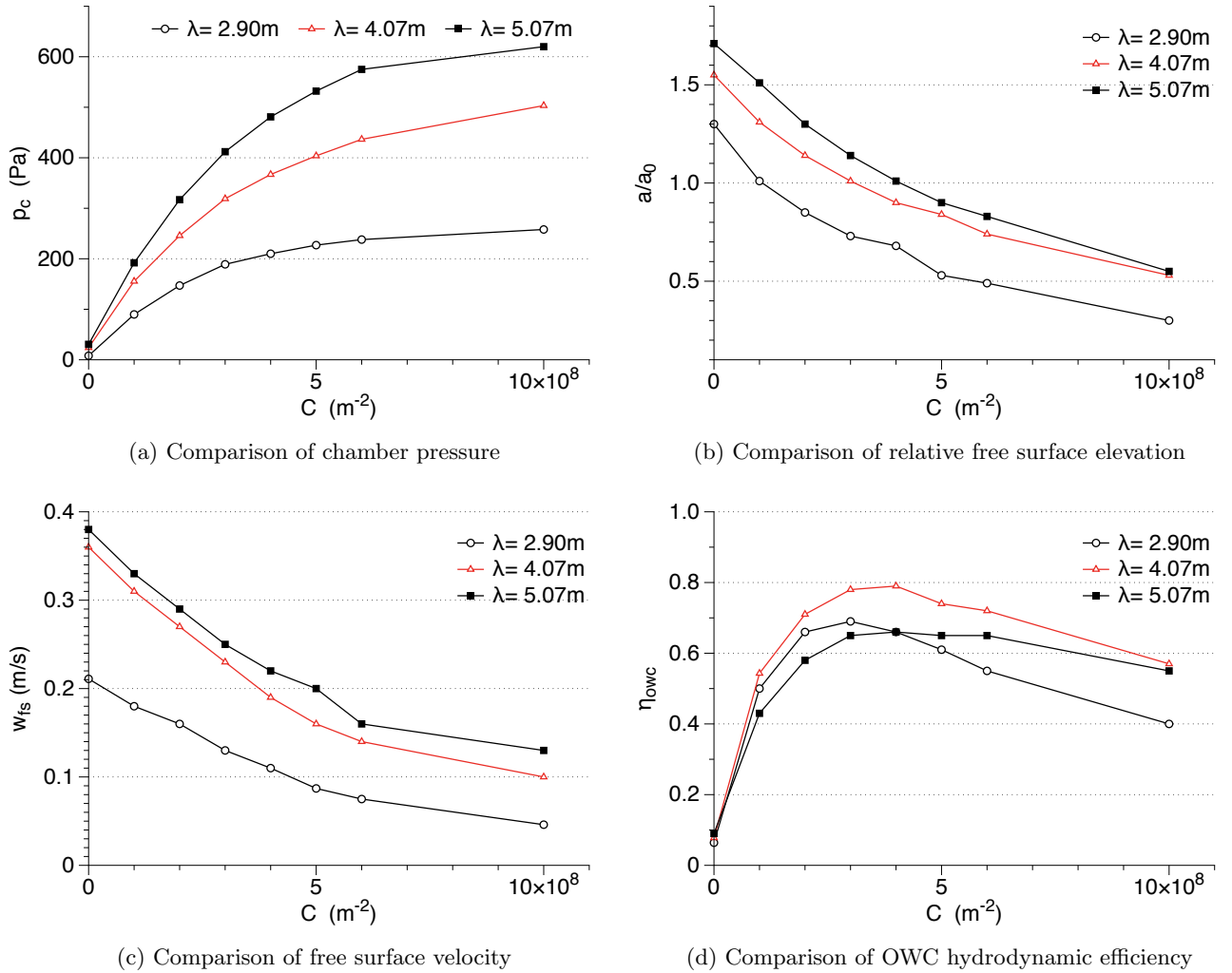


Figure 9: Variation of chamber pressure, relative free surface amplitude, free surface velocity and OWC hydrodynamic efficiency for different wavelengths under different values of C for a constant steepness $\xi = 0.03$

than the efficiency for $H = 0.06\text{m}$. The efficiency in the case of $\lambda = 5.07\text{m}$ is the lower than that seen for $H = 0.06\text{m}$ and $H = 0.12\text{m}$, as the wave height in this case is 0.152m . It is also observed that the maximum efficiency for $\lambda = 2.90\text{m}$, 4.07m and 5.07m are computed at C_3 , C_4 and C_5 respectively. These values remain the same for $H = 0.06\text{m}$, $H = 0.12\text{m}$ and $\xi = 0.03$. Thus, the maximum hydrodynamic efficiency at a particular incident wavelength is obtained at a particular value of PTO damping. The wavelength resulting in the maximum efficiency also remains the same under different values of PTO damping for a given geometry of the OWC. The OWC attains the maximum efficiency for shorter wavelengths at lower PTO damping and at a higher PTO damping for longer wavelengths. In the absence of PTO damping (C_0), the OWC fails to effectively deliver the incident wave energy to the vent. In this case, there is a large motion of the water column motion but the air column is not

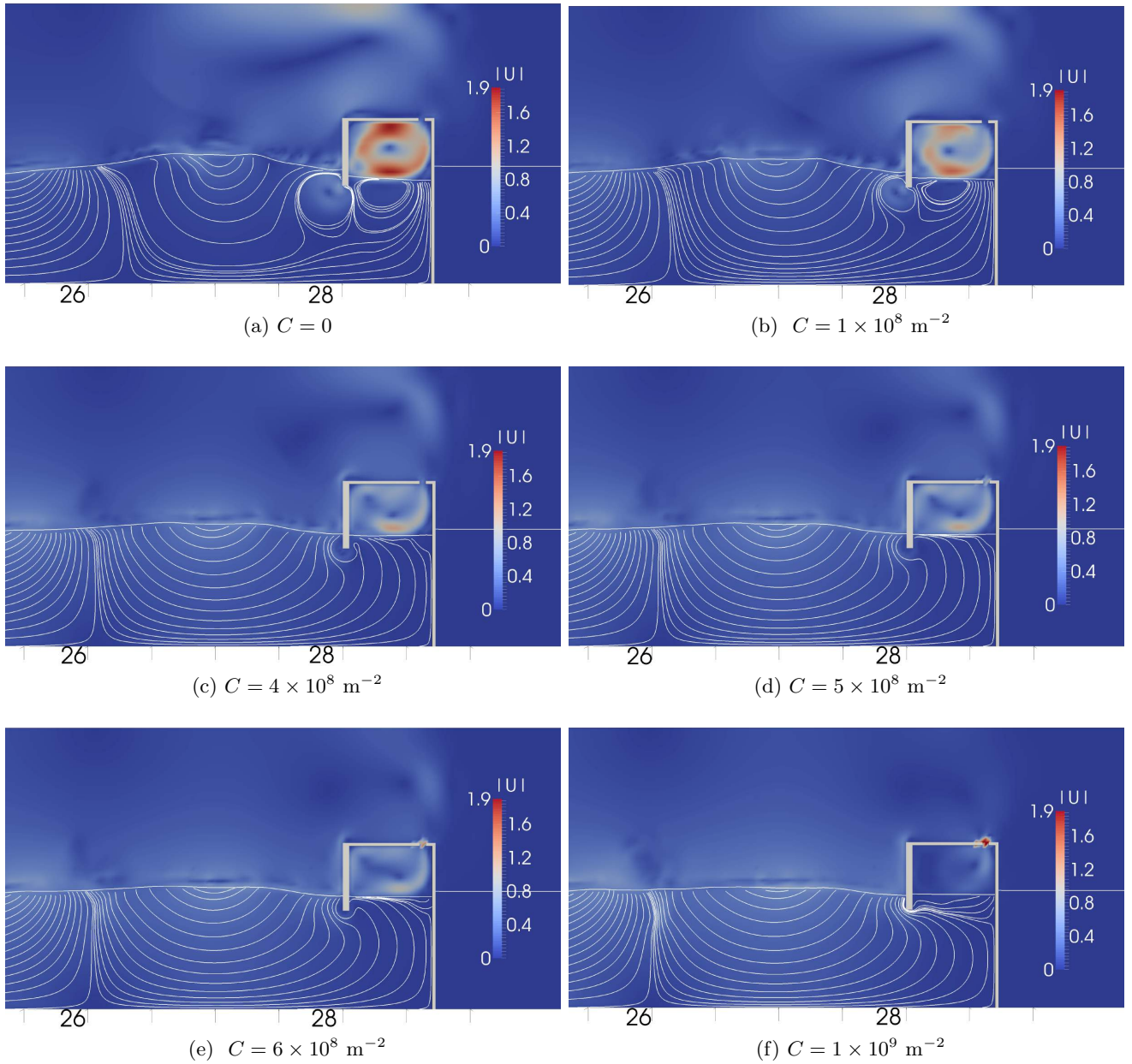


Figure 10: Streamlines in front of the device and free surface in the chamber for $\lambda = 4.07\text{m}$ for different values of C at $t/T = 12.56$

under sufficient pressure to result in meaningful work though its motion. The efficiency is also lowered in the case of very high PTO damping (C_{10}). This is justified by the fact that in a highly damped OWC chamber, the motion of the water column is extremely damped and the volume flux of air through the vent is reduced.

From the results presented above, the PTO damping has an influence on the chamber pressure, motion of the free surface in the chamber and the hydrodynamic efficiency of the

device. The influence of the PTO damping on the hydrodynamics of the device is further investigated by studying the streamlines in and around the OWC device for the incident wavelength of $\lambda = 4.07\text{m}$ for different values of C at the same time during the simulation. The development of large stagnation zones in the water is seen in Fig. 10a and 10b for C_0 and C_1 . A low PTO damping results in a low chamber pressure, a large amplitude of free surface oscillation and a high free surface velocity. Under these conditions, most of the wave energy is trapped in the large stagnation zones formed in and around the device. The size of the stagnation zones is reduced as the PTO damping on the chamber is increased in Fig. 10c, 10d, 10e and 10f. The increased PTO damping reduces the velocity of the free surface and a higher chamber pressure is developed. The optimum PTO damping creates conditions under which the hydrodynamic losses from stagnation zones and vortex formation in the water is reduced. Thus, a higher amount of the incident wave energy is available at the vent. This shows that the PTO damping on the device not only affects the conditions inside the chamber, but has significant effects on the hydrodynamics of the device and its interaction with the surrounding environment.

Thus, in the modeling, design and optimization of an OWC wave energy converter, the effect of the PTO damping should be taken into consideration as it affects the prevalent conditions inside the chamber and the hydrodynamics around the device. Also, the PTO damping could be adjusted according to the wave climate to tune the device for maximum hydrodynamic efficiency under the incident wave conditions.

6 Conclusions

A CFD model is used to study the effect of PTO damping on the OWC chamber in a two-dimensional numerical wave tank. Darcy's law for flow through porous media is used to model the PTO damping on the device chamber. The numerical model is validated by comparing the variation of the pressure, the free surface and the velocity of the free surface in the device chamber with experimental data from Morris-Thomas *et al.* (2007). The size of the vent in the OWC device in the numerical model is kept large enough so that the damping provided by it is extremely low while preserving the geometry of the device used in the experiments. So, the PTO damping is solely represented using the porous media in the vent of the OWC. The influence of PTO damping on the chamber pressure, free surface motion inside the chamber and the efficiency of the device for different incident wave heights and wavelengths is investigated and the following conclusions are drawn:

- increasing the PTO damping leads to a higher chamber pressure, lower free surface motion and lower velocity of the free surface motion for all the incident wavelengths.
- hydrodynamic efficiency increases with increasing PTO damping, reaches a maximum value and reduces on a further increase in PTO damping.
- maximum hydrodynamic efficiency for a given wavelength occurs at a particular value of PTO damping.
- the PTO damping resulting in maximum efficiency increases with increasing wavelength.
- the hydrodynamic efficiency decreases with increasing incident wave height.

- large stagnation zones are formed in front of the OWC and inside the chamber at lower PTO damping, which trap the wave energy and reduce the efficiency of the OWC.
- an optimum value of PTO damping results in a reduction in the size of the stagnation zones, with sufficient motion of the pressurised air column in the OWC chamber producing the maximum hydrodynamic efficiency.
- maximum hydrodynamic efficiency of an OWC can be achieved by tuning the PTO damping with respect to the incident waves. This increases the efficiency at incident wavelengths away from the resonant wavelength.

Thus, the PTO damping has a large influence on the hydrodynamics of an OWC and this can be used to attain the maximum possible hydrodynamic efficiency for a given incident wavelength. These results at a model scale do not include the effects of air compressibility. Further studies can be carried out at a large scale to account for air compressibility and also develop a formal relationship between the PTO damping and the OWC hydrodynamic efficiency.

Acknowledgements

The authors thank Michael Morris-Thomas, Principal Naval Architect, Worley Parsons, Perth, Australia for the experimental data and helpful discussions. This study has been carried out under the OWCBC project (No. 217622/E20) and the authors are grateful to the grants provided by the Research Council of Norway. This study was supported in part with computational resources at the Norwegian University of Science and Technology (NTNU) provided by NOTUR, <http://www.notur.no>.

References

- Alagan Chella, M., Bihs, H., Myrhaug, D. and Muskulus, M. (2015). Breaking characteristics and geometric properties of spilling breakers over slopes. *Coastal Engineering*, **95**, 4–19.
- Berthelsen, P.A. and Faltinsen, O.M. (2008). A local directional ghost cell approach for incompressible viscous flow problems with irregular boundaries. *Journal of Computational Physics*, **227**, 4354–4397.
- Bradshaw, P., Ferriss, D.H. and Atwell, N.P. (1967). Calculation of boundary layer development using the turbulent energy equation. *Journal of Fluid Mechanics*, **28**, 593–616.
- Chorin, A. (1968). Numerical solution of the Navier-Stokes equations. *Mathematics of Computation*, **22**, 745–762.
- Didier, E., Paixão Conde, J.M. and Teixeira, P.R.F. (2011). Numerical simulation of an oscillating water column wave energy convertor with and without damping. In: *Proc., International Conference on Computational Methods in Marine Engineering*, 206–217.
- Durbin, P.A. (2009). Limiters and wall treatments in applied turbulence modeling. *Fluid Dynamics Research*, **41**, 1–18.

- Egorov, Y. (2004). Validation of CFD codes with PTS-relevant test cases. Technical Report 5th Euratom framework programme ECORA project, EVOL-ECORA D07.
- Engsig-Karup, A.P. (2006). *Unstructured nodal DG-FEM solution of high-order boussinesq-type equations*. Ph.D. thesis, Technical University of Denmark, Lyngby.
- Evans, D.V. (1978). Oscillating water column wave energy convertors. *IMA Journal of Applied Mathematics*, **22**, 423–433.
- Evans, D.V. (1982). Wave power absorption by systems of oscillating surface pressure distributions. *Journal of Fluid Mechanics*, **114**, 481–499.
- Falcão, A.F.de.O. and Henriques, J.C.C. (2014). Model-prototype similarity of oscillating-water-column wave energy converters. *International Journal of Marine Energy*, **6**, 18–34.
- Jacobsen, N.G., Fuhrman, D.R. and Fredsøe, J. (2012). A wave generation toolbox for the open-source CFD library: OpenFOAM. *International Journal for Numerical Methods in Fluids*, **70**(9), 1073–1088.
- Jiang, G.S. and Peng, D. (2000). Weighted ENO schemes for Hamilton-Jacobi equations. *SIAM Journal on Scientific Computing*, **21**, 2126–2143.
- Jiang, G.S. and Shu, C.W. (1996). Efficient implementation of weighted ENO schemes. *Journal of Computational Physics*, **126**, 202–228.
- Larsen, J. and Dancy, H. (1983). Open boundaries in short wave simulations - a new approach. *Coastal Engineering*, **7**, 285–297.
- López, I., Pereiras, B., Castro, F. and Iglesias, G. (2014). Optimisation of turbine-induced damping for an OWC wave energy converter using a RANS-VOF numerical model. *Applied Energy*, **127**, 105–114.
- Mayer, S., Garapon, A. and Sørensen, L.S. (1998). A fractional step method for unsteady free surface flow with applications to non-linear wave dynamics. *International Journal for Numerical Methods in Fluids*, **28**, 293–315.
- Morris-Thomas, M.T., Irvin, R.J. and Thiagarajan, K.P. (2007). An investigation into the hydrodynamic efficiency of an oscillating water column. *Journal of Offshore Mechanics and Arctic Engineering*, **129**, 273–278.
- Peng, D., Merriman, B., Osher, S., Zhao, H. and Kang, M. (1999). A PDE-based fast local level set method. *Journal of Computational Physics*, **155**, 410–438.
- Sarmiento, A.J.N.A. (1992). Wave flume experiments on two-dimensional oscillating water column wave energy devices. *Experiments in Fluids*, **12**, 286–292.
- Sarmiento, A.J.N.A. and Falcão, A.F.de.O. (1985). Wave generation by an oscillating surface pressure and its application in wave energy extraction. *Journal of Fluid Mechanics*, **150**, 467–485.
- Shu, C.W. and Osher, S. (1988). Efficient implementation of essentially non-oscillatory shock capturing schemes. *Journal of Computational Physics*, **77**, 439–471.

- Thiruvankatasamy, K. and Neelamani, S. (1997). On the efficiency of wave energy caissons in array. *Applied Ocean Research*, **19**, 61–72.
- van der Vorst, H. (1992). BiCGStab: A fast and smoothly converging variant of Bi-CG for the solution of nonsymmetric linear systems. *SIAM Journal on Scientific and Statistical Computing*, **13**, 631–644.
- Wilcox, D.C. (1994). *Turbulence modeling for CFD*. DCW Industries Inc., La Canada, California.